

OPEN

Synchrotron-based high-resolution photoemission spectroscopy study of ZIRLO cladding with H₂O adsorption: Coverage and temperature dependence

Sangjune Park¹, Ki-jeong Kim², Jeongmook Lee³, Jong-Yun Kim^{3,4}, Dong Woo Lee³, Sang Ho Lim^{3,4*} & Young-Sang Youn^{1*}

The coverage and temperature dependence of ZIRLO cladding with H₂O adsorption are studied using synchrotron-based high-resolution photoemission spectroscopy (HRPES). Based on the analytical results of the Zr 3*d*, O 1*s*, C 1*s*, and Sn 3*d* HRPES profiles prior to H₂O adsorption, we determine the surface compositions of O²⁻, hydroxyl OH⁻, chemisorbed H₂O, zirconium carbide, adventitious carbon, Sn metal, and SnO₂ in ZIRLO. When ZIRLO is exposed to H₂O molecules, the relative proportion of zirconium metal decreases, whereas that of the total zirconium oxides increases, suggesting the reaction between H₂O and the zirconium metal in ZIRLO. On annealing a sample with 1000 L H₂O on ZIRLO at 300 °C, Zr₂O₃ and ZrO₂ decompose, and oxygen diffuses into the bulk, thereby reducing the oxidation states of zirconium on the surface. Moreover, at this temperature, the excess H₂O molecules on ZIRLO are thoroughly desorbed and tin element is diffused into the bulk in ZIRLO.

Zirconium and its alloys have been extensively used as cladding and structural materials in the nuclear industry because they possess several advantages over other materials, a low thermal neutron absorption cross-section, and good corrosion resistance, in particular^{1–3}.

Cladding is mainly composed of 95% or more zirconium, and serves to completely seal the nuclear fuels in the fuel rod to prevent the external release of fission products generated from nuclear fuels by irradiation^{4–7}. Several commercial claddings such as ZIRLO, ZIRCALOY-4, ZIRCALOY-2, and M5 are utilized in nuclear reactors. In order to generate electrical energy, they are always contacted with water to transfer the heat energy produced from the nuclear fuels to water⁸. Consequently, oxidation of the cladding surface by water is inevitable. Because this oxidation degrades the cladding performance, the reaction between the cladding and water should be studied to understand the oxidation phenomenon on the cladding surface.

ZIRLO, which is a commercially available cladding material, is fabricated with small quantities of niobium, tin, and iron, which are minor alloying elements, to improve the corrosion resistance and mechanical strength^{3,9}. Although the oxidation of pure zirconium, ZIRCALOY-2, ZIRCALOY-4, and M5 are actively researched, studies focusing on the ZIRLO cladding are rare^{1–3,8,10–18}. As ZIRLO is the most commonly used cladding material in the pressurized water reactors (PWRs), currently, investigating the oxidation behavior of ZIRLO by water is crucial to comprehend the oxidation behavior in current PWRs.

In view of the above, we performed experiments on the coverage and temperature dependence of ZIRLO cladding with H₂O adsorption using synchrotron-based high-resolution photoemission spectroscopy (HRPES), in this study. Because synchrotron-based HRPES renders it possible to change the photon energy, we can obtain

¹Department of Chemistry, Yeungnam University, Daehak-ro 280, Gyeongsan, Gyeongbuk, 38541, Republic of Korea.

²Pohang Accelerator Laboratory, Pohang University of Science and Technology, 80 Jogokro-127-beongil, Nam-gu, Pohang, Gyeongbuk, 37673, Republic of Korea. ³Nuclear Chemistry Research Team, Korea Atomic Energy Research Institute, 111, Daedeok-daero 989beon-gil, Yuseong-gu, Daejeon, 34057, Republic of Korea. ⁴Radiochemistry & Nuclear Nonproliferation, University of Science & Technology, Gajeong-ro 217, Yuseong-gu, Daejeon, 34113, Republic of Korea. *email: slim@kaeri.re.kr; ysyou@yu.ac.kr

a highly surface-sensitive signal from ZIRLO based on the universal curve¹⁹. We determined that even before the deposition of H₂O, the Zr 3*d* HRPES profile obtained from ZIRLO exhibited several peaks related to the Zr⁰, Zr⁺, Zr²⁺, Zr³⁺, and Zr⁴⁺ oxidation states, indicating that the surface of ZIRLO comprises zirconium metal and zirconium oxides. After the exposure of ZIRLO to H₂O, the relative quantity of zirconium metal decreased, whereas the total zirconium oxide quantity including Zr⁺, Zr²⁺, Zr³⁺, and Zr⁴⁺ relatively increased. Sequentially, we annealed a sample with H₂O adsorbed on ZIRLO to check the temperature dependence. On annealing up to 100 °C, there were no significant changes, whereas after annealing beyond 300 °C, the relative proportion of zirconium metal increased, and the relative quantities of the total zirconium oxides reduced with the decrease in Zr³⁺ and Zr⁴⁺ because of the decomposition of Zr₂O₃ and ZrO₂ accompanied by oxygen diffusion into the bulk, in agreement with literature^{10,20}. To the best of our knowledge, the coverage and temperature dependence of ZIRLO cladding with H₂O adsorption have not been systematically studied using synchrotron-based HRPES.

Materials and methods

To prepare a sample for the synchrotron-based HRPES experiments, ZIRLO (Westinghouse Electric Co.) with an area of approximately 10 × 10 mm² was polished with 3000 grit SiC paper, and rinsed with deionized water. This ZIRLO sample contained 1.27 wt% niobium, 1.13 wt% tin, and 0.11 wt% iron with very small quantities of oxygen, carbon, nitrogen, and hydrogen as reported elsewhere³. Deionized water (H₂O) was prepared using a Milli-Q water purification system (Millipore), and was further purified through several freeze-pump-thaw cycles to remove all the dissolved gases prior to deposition. The amount of H₂O exposure is expressed in Langmuir (L) which is calculated as the product of the H₂O molecule pressure and the exposure time (1 L = 10⁻⁶ Torr·s).

HRPES data were obtained using the 8A2 beamline at the Pohang accelerator laboratory (PAL). In an ultra-high vacuum (UHV) chamber in which the HRPES system was installed, ZIRLO was further cleaned through five cycles of sputtering with 0.5 keV Ar⁺ ions for 1 h at 380 °C, followed by annealing at 600 °C for 30 min. Although we attempted to completely eliminate the C 1*s* peak in the ZIRLO cladding, it continued to remain after five cycles of sputtering and annealing, similar to that reported in a previous study on ZIRCALOY-4 cladding^{10,21}. Therefore, this cycle of sputtering and annealing was stopped when the intensity of the C 1*s* peak no longer varied. All the core-level spectra of the sample with H₂O adsorbed on ZIRLO were recorded at room temperature using a high-performance electron analyzer (SCIENTA2002, Sienta-Omicron) at photon energies of 400, 630, and 710 eV for Zr 3*d*, and 710 eV for O 1*s*, C 1*s*, and Sn 3*d*, where the total spectral resolution at each photon energy was 0.15 eV, determined by measuring Au Fermi-edge. HRPES data were obtained with a pass energy of 20 eV for Zr 3*d* and 50 eV for O 1*s*, C 1*s*, and Sn 3*d* at an energy step of 0.05 eV. The binding energies of the core-level spectra were relatively calibrated with respect to that of the 4*f*_{7/2} HRPES spectrum (84.0 eV) of clean Au for the same photon energy. The base pressure of the UHV chamber was maintained below 5.0 × 10⁻¹⁰ Torr. All the spectra were measured in the normal-emission mode, and analyzed using a standard nonlinear least squares fitting procedure with Voigt functions²².

Results and discussion

Fig. 1 shows the Zr 3*d*, O 1*s*, C 1*s*, and Sn 3*d* HRPES spectra obtained from ZIRLO before the deposition of H₂O. Previous study reveals that tin element alone was detected by X-ray photoelectron spectroscopy (XPS), among the minor alloying elements present in ZIRCALOY-4 cladding¹⁰. When we performed preliminary experiments using commercial XPS (VG Scientific ESCALAB 220i-XL), the Fe 2*p* and Nb 3*d* peaks were not observed in ZIRLO; moreover, the Nb 3*d* signal was not detected in our HRPES spectrum. Therefore, to enhance the surface sensitivity without considering the detection of the Fe 2*p* signal, we lowered the photon energy as much as possible, resulting in a photon energy of 710 eV. Furthermore, as the primary analysis in this study involves the Zr 3*d* spectra, we reduced the photon energy up to 400 eV to obtain the most sensitive Zr 3*d* HRPES profiles. Fig. 1a displays the Zr 3*d* spectra acquired at photon energies of 400, 630, and 710 eV, respectively. The Zr 3*d* profiles obtained at photon energies of 630 and 710 eV were similar; however, that obtained at 400 eV was different. The electron inelastic-mean-free-paths (IMFPs) at photon energies of 400, 630, and 710 eV for Zr 3*d*, and 710 eV for C 1*s* and Sn 3*d* were calculated to be 7.1, 11.4, and 12.8 Å, and 14.2 and 8.3 Å, respectively, using the NIST electron inelastic-mean-free-path database (Version 1.2) with an algorithm developed by Tanuma, Powell, and Penn^{23,24}. In addition, the IMFP at photon energy of 710 eV for O 1*s* was approximately estimated as 7 Å using the universal curve¹⁹. In particular, the IMFPs for Zr 3*d* indicates that the spectrum at a photon energy of 400 eV contains more surface information compared to the others. Therefore, only the Zr 3*d* spectrum measured at a photon energy of 400 eV will be considered henceforth. The detailed analysis of the Zr 3*d* spectra with the peak fitting results is presented in Fig. 2.

Fig. 1b displays the O 1*s* HRPES profiles, in which three peaks can be observed: O1 at 530.0 eV, O2 at 531.4 eV, and O3 at 533.0 eV. The O1, O2, and O3 peaks are assigned to the O²⁻, hydroxyl OH⁻, and the chemisorbed H₂O features because the binding energies associated with them appear at 530.0–530.2 eV, 531.4 eV, and 533.4 eV, respectively, in literature^{25–27}. The C 1*s* HRPES profile is depicted in Fig. 1c, where two distinct peaks can be observed at 281.5 eV and 284.6 eV. We assigned the peak at 281.5 eV to zirconium carbide produced by the reaction between zirconium metal and the adsorbed hydrocarbon; this value is similar to the reported binding energy of 281.6–282.0 eV in previous investigations^{10,28}. In addition, the peak at 284.6 eV was assigned to adventitious carbon composed of various hydrocarbon species based on the previously reported value (284.6 eV)²⁹. As shown in Fig. 1c, the full width at half maximum (FWHM) of adventitious carbon at 284.6 eV is broader compared to that of zirconium carbide at 281.5 eV, which may be due to the existence of various types of hydrocarbons. In the Sn 3*d* HRPES profile (Fig. 1d), two types of Sn 3*d*_{5/2} peaks at 484.1 and 486.0 eV, and 3*d*_{3/2} signals at 492.5 and 494.4 eV, respectively, appeared with binding energy separation of 8.4 eV between them. In general, the binding energy of Sn 3*d*_{5/2} is used to analyze the Sn 3*d* HRPES profile. It is known that the binding energies of Sn metal and the SnO₂ features in ZIRCALOY-4 cladding occur between 483.9–484.7 eV and 486.0–487.2 eV, respectively^{10,18}.

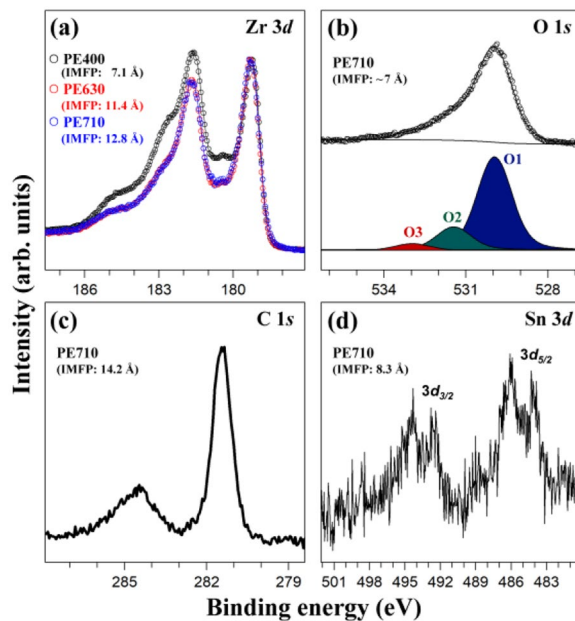


Figure 1. (a) Zr 3d, (b) O 1s, (c) C 1s, and (d) Sn 3d HRPES spectra obtained from ZIRLO before the deposition of H₂O, where PE means the photon energy (eV). Black, red, blue open circles in (a) indicate Zr 3d spectra acquired at the photon energies of 400, 630, and 710 eV, respectively, which were normalized using Zr 3d_{5/2} peak of zirconium metal at 179.3 eV. The dots and the solid lines in (b) represent the experimental values and the peak fitting results, respectively.

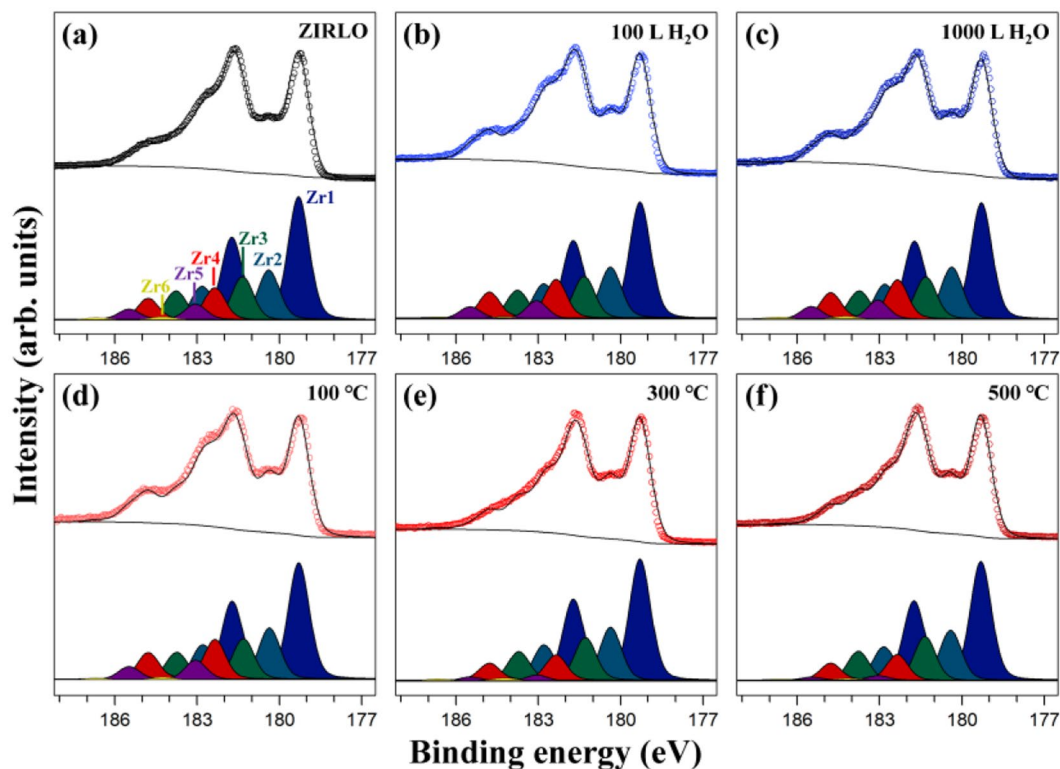


Figure 2. Zr 3d HRPES spectra of ZIRLO recorded at the photon energy of 400 eV (a) before the adsorption of H₂O, after the dosing of (b) 100 L and (c) 1000 L H₂O, and after annealing at (d) 100 °C, (e) 300 °C, and (f) 500 °C subsequent to the deposition of 1000 L H₂O. The open circles correspond to the experimental values, and the solid lines are obtained by peak fitting. The experimental data in (a) is the same with the spectrum obtained at the photon energy of 400 eV in Fig. 1a.

| | Zr ⁰ (%) | Zr ⁺ (%) | Zr ²⁺ (%) | Zr ³⁺ (%) | Zr ⁴⁺ (%) | Zr(OH) ₄ (%) |
|---------------------------------------|------------------------|------------------------|-------------------------|-------------------------|-------------------------|----------------------------|
| Before deposition of H ₂ O | 46.4 | 18.5 | 16.3 | 12.0 | 5.8 | 1.0 |
| 100 L H ₂ O deposition | 43.7 | 19.0 | 15.7 | 14.5 | 6.7 | 0.4 |
| 1000 L H ₂ O deposition | 43.1 | 19.2 | 15.5 | 14.4 | 7.0 | 0.8 |
| Annealing at 100 °C | 43.1 | 19.0 | 15.0 | 14.8 | 7.2 | 0.9 |
| Annealing at 300 °C | 48.3 | 21.3 | 17.0 | 10.1 | 2.4 | 0.9 |
| Annealing at 500 °C | 48.5 | 20.5 | 18.1 | 10.5 | 1.9 | 0.5 |

Table 1. Relative proportions of the zirconium species in ZIRLO calculated from each peak integral of the peak fitting results of Zr 3*d* HRPES spectra in Fig. 2.

Therefore, we assigned the two Sn 3*d*_{5/2} peaks at 484.1 and 486.0 eV to Sn metal and the SnO₂ compositions, respectively. Thus, by analyzing the HRPES spectra (Fig. 1) obtained from ZIRLO, we established the presence of O²⁻, hydroxyl OH⁻, chemisorbed H₂O, zirconium carbide, adventitious carbon, Sn metal, and the SnO₂ species.

The fact that such features appeared despite our cleaning process suggests that they may be due to the intrinsic oxygen and carbon in ZIRLO, which was also observed in prior XPS studies on ZIRCALOY-4 cladding^{10,21}.

Fig. 2a depicts the Zr 3*d* HRPES profile, shown in Fig. 1a, with the peak fitting results. Because the binding energy of Zr 3*d*_{5/2} is typically utilized to analyze the Zr 3*d* HRPES profile, we explain the zirconium species using the binding energy of Zr 3*d*_{5/2}. In Fig. 2a, six peaks can be observed: Zr1 at 179.3 eV, Zr2 at 180.4 eV, Zr3 at 181.3 eV, Zr4 at 182.4 eV, Zr5 at 183.1 eV, and Zr6 at 184.2 eV. We first assigned Zr1 at 179.3 eV and Zr5 at 183.1 eV to the Zr⁰ (zirconium metal) and Zr⁴⁺ (ZrO₂) features, respectively, based on their binding energies ranging from 179.1–179.3 eV and 182.9–183.4 eV in literature^{9,10,18,30}. In addition, it is known that the intervals of the binding energies between the Zr⁺, Zr²⁺, Zr³⁺, Zr⁴⁺ oxidation states are approximately 1 eV^{1,31,32}. Considering the binding energy of the Zr⁴⁺ feature (183.1 eV) in our system, we assigned Zr2 at 180.4 eV, Zr3 at 181.3 eV, and Zr4 at 182.4 eV to the Zr⁺ (Zr₂O), Zr²⁺ (ZrO), and Zr³⁺ (Zr₂O₃) compositions, respectively, which are zirconium suboxides. Moreover, Zr6 at 184.2 eV, of which a small quantity was present, was assigned to zirconium hydroxide (Zr(OH)₄) because its reported binding energy (183.6 eV) was similar to our value^{33,34}. Previously, through the analysis of the C 1*s* HRPES profile in Fig. 1c, we had established the existence of zirconium carbide in ZIRLO. According to literature, the binding energy of zirconium carbide in the Zr 3*d* spectrum is 179.2 eV^{10,28}, which is almost the same as that of zirconium metal (179.3 eV). Although the zirconium carbide component should be considered when the Zr 3*d* HRPES profile is analyzed, we could not confirm whether this peak was due to zirconium metal or zirconium carbide, in agreement with the previous report¹⁰. Hence, we had to unavoidably ascribe the peak at 179.3 eV to zirconium metal.

It has been previously revealed that the order of the surface components in intact ZIRCALOY-4 cladding are as follows: The uppermost hydrocarbon, zirconium hydroxide, zirconium dioxide, zirconium suboxides, and zirconium bulk layers¹⁰. In addition, zirconium carbide is expected to exist in the hydrocarbon layer. As a result, based on the analysis of the Zr 3*d*, O 1*s*, C 1*s*, and Sn 3*d* HRPES spectra, along with the prior report, we concluded that the surface species in ZIRLO cladding could be the same as previously reported. Additionally, we propose that Sn metal and SnO₂ compositions could exist within the zirconium bulk layer, and that the chemisorbed H₂O feature could be present in the uppermost layer.

To confirm the change in the relative proportions of the zirconium features depending on the H₂O coverage and annealing temperature, we calculated the ratio of each peak area obtained from the peak fitting results because the ratio of each peak integral in the Zr 3*d* HRPES spectra corresponds to their relative proportion (Table 1). As the proportion of zirconium hydroxide is negligible, we consider the other populations, herein. As shown in Fig. 2 and Table 1, the relative proportion of zirconium metal is the largest, and gradually decreases in the following order Zr⁺, Zr²⁺, Zr³⁺, and Zr⁴⁺, in accordance with their relative trends reported in literature¹. After the exposure of ZIRLO to 100 L and 1000 L H₂O, the relative proportion of zirconium metal decreased whereas those of the zirconium oxides including the Zr⁺, Zr²⁺, Zr³⁺, and Zr⁴⁺ features mostly increased (Fig. 2 and Table 1). This indicates that when H₂O is adsorbed on ZIRLO, H₂O and zirconium metal in ZIRLO react each other, relatively decreasing and increasing the metal population and the total quantity of zirconium oxides, respectively, in agreement with previous research on H₂O adsorbed on pure zirconium and ZIRCALOY-2 samples¹. This phenomenon can be explained by the dissociation of H₂O into the adsorbed oxygen and molecular hydrogen gas on ZIRLO at room temperature as reported in the prior study of water molecule on Zr(0001)³⁵. We performed annealing experiments on the 1000 L H₂O system adsorbed on ZIRLO. As shown in Fig. 2d, the Zr 3*d* HRPES profile after annealing at 100 °C for 30 min is similar to that before annealing, indicating that any detectable change did not occur due to annealing at this temperature. However, when temperatures of 300 °C and 500 °C were applied for 30 min, the relative percentage of the Zr⁰, Zr⁺, and Zr²⁺ valence states increased, whereas those of the Zr³⁺ and Zr⁴⁺ oxidation states decreased (Fig. 2e,f). According to literature, on annealing at 200 °C or more, the oxidation states of zirconium are converted to lower oxidation states because of the decomposition of the Zr₂O₃ and ZrO₂ compositions, and the depopulation of oxygen in the surface region accompanied by oxygen diffusion into the bulk^{10,20}. Therefore, we concluded that the decomposition of Zr₂O₃ and ZrO₂ and the diffusion of oxygen into the bulk lead to the reduction of the oxidation states of zirconium at 300 °C.

Fig. 3 displays the coverage and temperature dependence of the O 1*s* and Sn 3*d* HRPES profiles. As shown in Fig. 3a, after the adsorption of 100 L and 1000 L H₂O on ZIRLO, the peak related to chemisorbed H₂O notably

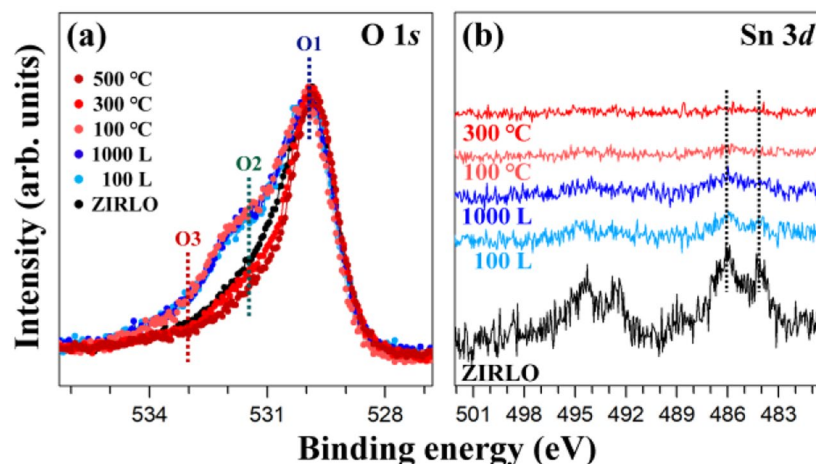


Figure 3. (a) O 1s and (b) Sn 3d HRPES spectra of ZIRLO measured before the deposition of H₂O, after the adsorption of 100 L and 1000 L H₂O, and after annealing at 100 °C, 300 °C, and 500 °C subsequent to the deposition of 1000 L H₂O. O 1s HRPES spectra in (a) were normalized using O1 peak at 530.0 eV. Sn 3d HRPES spectra obtained after annealing at up to 300 °C are exhibited in (b). The dashed lines express the positions of the binding energy of each feature.

increases. This increase is attributed to the excess H₂O molecules on ZIRLO, which could be the remaining quantity after sufficient reaction with zirconium metal. After annealing at 100 °C for 30 min, the profile of the O 1s HRPES spectrum remained unchanged, in accordance with the analytical result of the Zr 3d HRPES spectrum at this temperature. When the sample was annealed at 300 °C and 500 °C for 30 min, the enhanced peaks returned to the state before the adsorption of H₂O on ZIRLO, indicating that the excess H₂O molecules were completely desorbed at 300 °C. In the Sn 3d HRPES profiles (Fig. 3b), the peaks related to the Sn metal and SnO₂ compositions gradually disappear due to the deposition of 100 L and 1000 L H₂O on ZIRLO. As the adsorption of H₂O on ZIRLO increases the surface thickness, these signals may be reduced because the probing depth for ZIRLO itself relatively becomes shallow. After annealing at 100 °C for 30 min, only the peak at 486.0 eV related to the SnO₂ configuration remained indistinctly in the Sn 3d HRPES spectrum. Furthermore, after annealing at 300 °C for 30 min, it completely vanished instead of recovery, despite the desorption of H₂O molecules at this temperature. Therefore, we infer that SnO₂ composition decomposed and that Sn metal migrated into zirconium bulk at 300 °C, sequentially.

Conclusions

In this study, we investigated the coverage and annealing-temperature dependence of the ZIRLO cladding with H₂O adsorption using synchrotron-based HRPES. Through the analysis of the Zr 3d, O 1s, C 1s, and Sn 3d HRPES profiles obtained from ZIRLO before H₂O exposure, we confirmed the existence of O²⁻, hydroxyl OH⁻, chemisorbed H₂O, zirconium carbide, adventitious carbon, Sn metal, and SnO₂ species in ZIRLO. After the deposition of H₂O on ZIRLO, the relative proportion of zirconium metal decreased, whereas that of the total zirconium oxides increased, indicating that H₂O reacted with zirconium metal in ZIRLO. On annealing a sample with 1000 L H₂O adsorbed on ZIRLO at 300 °C, the decomposition of Zr₂O₃ and ZrO₂ as well as the diffusion of oxygen into the bulk occurred. Furthermore, we determined that the excess H₂O molecules were completely desorbed and that on SnO₂ decomposition, the tin element diffused into the zirconium bulk in ZIRLO at that temperature.

Received: 2 January 2020; Accepted: 1 April 2020;

Published online: 20 April 2020

References

1. Yoshitaka, N., Krauss, A. R., Yuping, L. & Gruen, D. M. Initial oxidation of zirconium and Zircaloy-2 with oxygen and water vapor at room temperature. *J. Nucl. Mater.* **228**, 346–353 (1996).
2. Stojilovic, N., Bender, E. T. & Ramsier, R. D. High-temperature Auger electron spectroscopy of Zircaloy-4. *Appl. Surf. Sci.* **252**, 1806–1811 (2005).
3. Youn, Y.-S., Park, J. & Lim, S. H. Stable lattice thermal expansion of ZIRLO™: High-temperature X-ray diffraction results. *J. Nucl. Mater.* **523**, 66–70 (2019).
4. Rondinella, V. V. & Wiss, T. The high burn-up structure in nuclear fuel. *Mater. Today* **13**, 24–32 (2010).
5. Ewing, R. C. Long-term storage of spent nuclear fuel. *Nat. Mater.* **14**, 252 (2015).
6. Konings, R. J. M., Wiss, T. & Beneš, O. Predicting material release during a nuclear reactor accident. *Nat. Mater.* **14**, 247 (2015).
7. Youn, Y.-S., Lee, J., Kim, J. & Kim, J.-Y. Compositional changes at the interface between thorium-doped uranium dioxide and zirconium due to high-temperature annealing. *J. Nucl. Mater.* **504**, 50–54 (2018).
8. Stojilovic, N. & Ramsier, R. D. Oxidation of Zircaloy-4 by H₂O followed by molecular desorption. *Appl. Surf. Sci.* **252**, 5839–5845 (2006).
9. Park, J., Jung, S.-W., Chun, M.-S. & Kang, Y.-C. Surface phenomena of deuterized ethanol exposed Zircaloy-4 surfaces. *Bull. Korean Chem. Soc.* **30**, 1349–1352 (2009).

10. Kaufmann, R. *et al.* XPS studies of the thermal behaviour of passivated Zircaloy-4 surfaces. *Surf. Interface Anal.* **11**, 502–509 (1988).
11. Barberis, P. Zirconia powders and Zircaloy oxide films: tetragonal phase evolution during 400 °C autoclave tests. *J. Nucl. Mater.* **226**, 34–43 (1995).
12. Bai, X. D. *et al.* Effect of self-ion bombardment damage on high temperature oxidation behavior of Zircaloy-4. *J. Nucl. Mater.* **254**, 266–270 (1998).
13. Lyapin, A., Jeurgens, L. P. H. & Mittemeijer, E. J. Effect of temperature on the initial, thermal oxidation of zirconium. *Acta Mater.* **53**, 2925–2935 (2005).
14. Park, D. J., Park, J. Y. & Jeong, Y. H. Microstructural analysis and XPS investigation of nodular oxides formed on Zircaloy-4. *J. Nucl. Mater.* **412**, 233–238 (2011).
15. Steinbrück, M. & Böttcher, M. Air oxidation of Zircaloy-4, M5[®] and ZIRLO[™] cladding alloys at high temperatures. *J. Nucl. Mater.* **414**, 276–285 (2011).
16. Idarraga, I., Mermoux, M., Duriez, C., Crisci, A. & Mardon, J. P. Raman investigation of pre- and post-breakaway oxide scales formed on Zircaloy-4 and M5[®] in air at high temperature. *J. Nucl. Mater.* **421**, 160–171 (2012).
17. Bespalov, I. *et al.* Initial stages of oxide formation on the Zr surface at low oxygen pressure: An *in situ* FIM and XPS study. *Ultramicroscopy* **159**, 147–151 (2015).
18. Xie, S. *et al.* A novel mechanism for nodular corrosion of Zircaloy-4 corroded in 773K superheated steam. *Corros. Sci.* **126**, 44–54 (2017).
19. Seah, M. P. & Dench, W. A. Quantitative electron spectroscopy of surfaces: A standard data base for electron inelastic mean free paths in solids. *Surf. Interface Anal.* **1**, 2–11 (1979).
20. Oh, K.-S. & Kang, Y.-C. The effects of Ar-ion bombardment and annealing of D2O/Zircaloy-4 surfaces using XPS and UPS. *Bull. Korean Chem. Soc.* **28**, 1341–1345 (2007).
21. Jung, H. Y. & Kang, Y.-C. Investigation of NH₄OH on Zircaloy-4 surfaces using electron emission spectroscopy. *Bull. Korean Chem. Soc.* **28**, 1751–1755 (2007).
22. Schreier, F. The Voigt and complex error function: A comparison of computational methods. *J. Quant. Spectrosc. Radiat. Transfer* **48**, 743–762 (1992).
23. Tanuma, S., Powell, C. J. & Penn, D. R. Calculations of electron inelastic mean free paths. II. *Data for 27 elements over the 50–2000 eV range.* *Surf. Interface Anal.* **17**, 911–926 (1991).
24. Tanuma, S., Powell, C. J. & Penn, D. R. Calculations of electron inelastic mean free paths. V. Data for 14 organic compounds over the 50–2000 eV range. *Surf. Interface Anal.* **21**, 165–176 (1994).
25. Olsson, C. O. A. & Landolt, D. Atmospheric oxidation of a Nb–Zr alloy studied with XPS. *Corros. Sci.* **46**, 213–224 (2004).
26. Jeon, M. K., Choi, Y. T., Lee, C. H., Kang, K. H. & Park, G. I. Surface analysis study on ZIRLO cladding hulls oxidized at low temperatures. *J. Nucl. Fuel Cycle Waste Technol.* **12**, 235–243 (2014).
27. Peng, D. Q., Bai, X. D. & Chen, B. S. Corrosion behavior of carbon implanted ZIRLO alloy in 1 M H₂SO₄. *J. Mater. Sci.* **40**, 1169–1175 (2005).
28. Craciun, D., Socol, G., Stefan, N., Bourne, G. & Craciun, V. Chemical composition of ZrC thin films grown by pulsed laser deposition. *Appl. Surf. Sci.* **255**, 5260–5263 (2009).
29. Barr, T. L. & Seal, S. Nature of the use of adventitious carbon as a binding energy standard. *J. Vac. Sci. Technol., A* **13**, 1239–1246 (1995).
30. Kumari, L. *et al.* Controlled Hydrothermal Synthesis of Zirconium Oxide Nanostructures and Their Optical Properties. *Crystal Growth & Design* **9**, 3874–3880 (2009).
31. Morant, C., Sanz, J. M., Galán, L., Soriano, L. & Rueda, F. An XPS study of the interaction of oxygen with zirconium. *Surf. Sci.* **218**, 331–345 (1989).
32. Liao, W., Zheng, T., Wang, P., Tu, S. & Pan, W. Efficient microwave-assisted photocatalytic degradation of endocrine disruptor dimethyl phthalate over composite catalyst ZrOx/ZnO. *J. Environ. Sci.* **22**, 1800–1806 (2010).
33. Barr, T. L. An ESCA study of the termination of the passivation of elemental metals. *J. Phys. Chem.* **82**, 1801–1810 (1978).
34. Huang, C., Tang, Z. & Zhang, Z. Differences between Zirconium Hydroxide (Zr(OH)₄·nH₂O) and Hydrous Zirconia (ZrO₂·nH₂O). *J. Am. Ceram. Soc.* **84**, 1637–1638 (2001).
35. Li, B., Griffiths, K., Zhang, C. S. & Norton, P. R. The autocatalytic decomposition of water on Zr(0001). *Surf. Sci.* **384**, 70–80 (1997).

Acknowledgements

This research was supported by the National Research Foundation of Korea (NRF) funded by the Korean government (MSIP) (Grant No. 2017M2A8A5014754 and 2019M1A7A1A02085179). This work was also supported by Dongil Culture and Scholarship Foundation research grant in 2019. Experiments at PLS-II were supported in part by MSICT and POSTECH, and NRF-2018R1D1A1B07048177.

Author contributions

Y.-S.Y. and J.-Y.K. conceived and designed the experiments. K.K. and Y.-S.Y. performed the experiments. S.P. and Y.-S.Y. analyzed the HRPES data. J.L., S.H.L., and Y.-S.Y. wrote the manuscript. D.W.L. critically contributed to revising the manuscript during the revision stage. All authors reviewed and approved the final manuscript.

Competing interests

The authors declare no competing interests.

Additional information

Correspondence and requests for materials should be addressed to S.H.L. or Y.-S.Y.

Reprints and permissions information is available at www.nature.com/reprints.

Publisher's note Springer Nature remains neutral with regard to jurisdictional claims in published maps and institutional affiliations.



Open Access This article is licensed under a Creative Commons Attribution 4.0 International License, which permits use, sharing, adaptation, distribution and reproduction in any medium or format, as long as you give appropriate credit to the original author(s) and the source, provide a link to the Creative Commons license, and indicate if changes were made. The images or other third party material in this article are included in the article's Creative Commons license, unless indicated otherwise in a credit line to the material. If material is not included in the article's Creative Commons license and your intended use is not permitted by statutory regulation or exceeds the permitted use, you will need to obtain permission directly from the copyright holder. To view a copy of this license, visit <http://creativecommons.org/licenses/by/4.0/>.

© The Author(s) 2020